


ARTICLE

DOI: 10.1038/s41467-018-07417-1

OPEN

Structure of DNA-CMG-Pol epsilon elucidates the roles of the non-catalytic polymerase modules in the eukaryotic replisome

Panchali Goswami¹, Ferdos Abid Ali¹, Max E. Douglas², Julia Locke¹, Andrew Purkiss³, Agnieszka Janska², Patrik Eickhoff¹, Anne Early², Andrea Nans³, Alan M. C. Cheung ^{4,5}, John F.X. Diffley² & Alessandro Costa¹

Eukaryotic origin firing depends on assembly of the Cdc45-MCM-GINS (CMG) helicase. A key step is the recruitment of GINS that requires the leading-strand polymerase Pol epsilon, composed of Pol2, Dpb2, Dpb3, Dpb4. While a truncation of the catalytic N-terminal Pol2 supports cell division, Dpb2 and C-terminal Pol2 (C-Pol2) are essential for viability. Dpb2 and C-Pol2 are non-catalytic modules, shown or predicted to be related to an exonuclease and DNA polymerase, respectively. Here, we present the cryo-EM structure of the isolated C-Pol2/Dpb2 heterodimer, revealing that C-Pol2 contains a DNA polymerase fold. We also present the structure of CMG/C-Pol2/Dpb2 on a DNA fork, and find that polymerase binding changes both the helicase structure and fork-junction engagement. Inter-subunit contacts that keep the helicase-polymerase complex together explain several cellular phenotypes. At least some of these contacts are preserved during Pol epsilon-dependent CMG assembly on path to origin firing, as observed with DNA replication reconstituted *in vitro*.

¹Macromolecular Machines Laboratory, The Francis Crick Institute, 1 Midland Road, London NW1 1AT, UK. ²Chromosome Replication Laboratory, The Francis Crick Institute, 1 Midland Road, London NW1 1AT, UK. ³Structural Biology Science Technology Platform, The Francis Crick Institute, 1 Midland Road, London NW1 1AT, UK. ⁴Department of Structural and Molecular Biology, Institute of Structural and Molecular Biology, University College London, London, UK. ⁵Institute of Structural and Molecular Biology, Biological Sciences, Birkbeck College, London WC1E 7HX, UK. These authors contributed equally: Panchali Goswami, Ferdos Abid Ali. Correspondence and requests for materials should be addressed to A.C. (email: alessandro.costa@crick.ac.uk)

DNA replication requires tight coordination between DNA unwinding and synthesis within the replisome¹. In eukaryotic cells, the replisome is assembled in three distinct steps leading to origin licensing, DNA untwisting, and replication fork establishment^{2–5}. First, the minichromosome maintenance protein complex (MCM) helicase, a ring-shaped ATPase, is loaded onto origins of replication as an inactive double hexamer that encircles duplex DNA^{6–9}, in a process that involves ATP hydrolysis by MCM^{10,11} and requires loading factors ORC, Cdc6, and Cdt1¹². Second, helicase activators Cdc45 and GINS are recruited in a regulated manner, mediated by targets of cyclin-dependent kinase (CDK) phosphorylation, Sld2 and Sld3, and by the replisome-maturation scaffolds, Dpb11 and Sld7. MCM phosphorylation by DDK allows Cdc45-Sld3-Sld7 binding to the double hexamer, dependent on phospho-MCM recognition by Sld3^{13–18}. GINS is recruited onto the MCM together with the leading-strand polymerase Pol epsilon, phospho-Sld2 and Dpb11, together forming the pre-loading complex¹⁹. Assembly of a stable Cdc45-MCM-GINS (CMG) holo-helicase requires a change in the MCM ATPase state, with release of ADP and binding of ATP, concomitantly promoting separation of the double hexamer into single hexamers and untwisting of duplex DNA². The third step in origin activation is replication fork establishment, which depends on the recruitment of additional firing factors Mcm10, RPA, and Pol alpha^{13,20}.

The organizing center of the replisome is the MCM²¹, made of six homologous polypeptides that all share the same domain organization. MCM proteins form an N-terminal duplex DNA-interacting collar and a AAA+ (ATPase associated with various cellular activities) tier, featuring bipartite active sites with catalytic residues contributed by neighboring subunits²². Work on *Drosophila* CMG revealed that the helicase motor is functionally asymmetric, as certain ATPase centers (Mcm2-5 and Mcm5-3) are strictly required for DNA unwinding, while other sites (Mcm6-4 and Mcm4-7) can be inactivated with minimal effect on helicase activity²³. Electron microscopy (EM) studies of both *Drosophila* and yeast CMG have revealed that Cdc45 and GINS (Sld5, Psf1, Psf2, Psf3) bind to the side of the MCM ring by engaging the N-terminal tier of MCM and stabilizing the Mcm2-5 and Mcm5-3 interfaces, respectively^{24–26}.

Reconstitution studies showed that the leading-strand polymerase Pol epsilon forms a stable complex with the CMG^{21,27}, by binding to the ATPase tier of MCM via a non-catalytic domain²⁸. Hetero-tetrameric Pol epsilon plays a key role in replisome maturation and origin activation^{19,29,30}. In this protein assembly, Dpb3 and Dpb4 are ancillary, DNA-binding subunits containing a histone fold³¹. Pol2 is the catalytic subunit, with the N-terminal half containing DNA synthesis/exonuclease functions³². The C-terminal half of Pol2 (C-Pol2) has been predicted to contain a second polymerase fold, which has become inactivated during evolution³³, and is followed by a zinc-finger appendix³⁴. Notably, the catalytic domain of Pol epsilon is dispensable for viability (though cells are sick), while the non-catalytic C-Pol2 is essential^{35,36}. Dpb2, the second largest subunit of Pol epsilon, is also essential for viability and contains an inactivated calcineurin-like exonuclease fold³⁴ decorated by an N-terminal appendix structurally related to the AAA+ ATPase lid domain³⁷. It is clear that non-catalytic modules in Pol epsilon are required for helicase activation and origin firing^{13,35,38}, although the molecular basis is poorly understood. Furthermore, what role these inactivated domains play during fork progression is unclear¹. To explain the functions of the leading-strand polymerase during DNA replication, we determined the structure of the non-catalytic modules of Pol epsilon by cryo-EM and biochemically assayed their DNA-binding properties. We have also determined the structure of Pol epsilon bound to a DNA-fork-engaged CMG complex to gain

insights into the architecture of the replisome during fork progression. We found that non-catalytic Pol epsilon causes a conformational change within the MCM ATPase, affecting the CMG interaction with the replication fork nexus. Based on predictions from the DNA-CMG-Pol epsilon structure, we identified the minimal complement of Pol epsilon modules required for assembling the CMG, by using the in vitro reconstituted DNA replication system. Therefore, certain protein–protein interactions important for CMG assembly during origin activation appear to be preserved in the CMG-Pol epsilon complex reconstituted on the replication fork. Together, our data provide important insights into the distinct roles of Pol epsilon during DNA replication.

Results

Structure of the Pol epsilon modules essential for viability. To understand the role of the essential Pol epsilon modules during DNA replication, we studied the structure of a truncation mutant of the yeast tetrameric complex, lacking the dispensable, flexibly tethered N-terminal catalytic domain of Pol2²⁸ (hereafter, delta-cat, Fig. 1a). Our first attempts to trap particles in vitreous ice resulted in severe aggregation, probably as a consequence of particle exposure to the air–water interface. To mitigate this problem, we incubated our preparation with 0.01% of cross-linking agent glutaraldehyde for one minute on ice, before cryo-grid making (Supplementary Fig. 1). The resulting particles appeared homogeneous and monodisperse. We deemed this preparation suitable for image acquisition on a Titan Krios EM equipped with a Falcon III direct electron detector operated in counting mode. Given the relatively small size of our protein target and inherent flexibility detected in preliminary cryo-EM characterization²⁸, we acquired a dataset at low defocus and using the Volta phase plate (VPP). As image contrast in these conditions is dramatically improved, high-resolution structures can be obtained using significantly fewer particles compared to defocus-based phase-shift imposition. This strategy provides an important advantage when dealing with inherently flexible particles³⁹. Two-dimensional averages showed high-resolution features for several particle orientations, with one prominent view revealing an anchor-shaped structure (Fig. 1b and Supplementary Fig. 1). A poorly resolved feature could be detected and deeper 2D classification efforts revealed a structured domain flexibly tethered to the particle core (Supplementary Movie 1). We determined a 3D structure of the delta-cat core based on 161,372 particles, to an average resolution of 4.45 Å (4.3 Å in the core and 5 Å in the periphery), revealing a compact assembly of dimensions 100 × 90 × 60 Å (Fig. 1c and Supplementary Fig. 1–2). To interpret the map, we have docked a recently published structure of human C-terminal Dpb2 bound to the Pol2 C-terminal zinc-finger appendix³⁴, providing an unambiguous fit. A yeast homology model based on the human structure was subsequently used as a template for real-space refinement (Fig. 1d–e). The residual density displayed an obvious resemblance to a DNA polymerase fold and homology searches performed with HHpred⁴⁰ indicated that the DNA polymerase domain of Pol1, from the tetrameric Pol alpha/primase complex⁴¹, is a suitable model for C-Pol2 (Fig. 2a). Docking of a Pol1-based homology model of C-Pol2 into the cryo-EM density required splitting the polymerase into three domains, which were used in independent rigid-body fitting and subsequent real-space refinement. The resulting structure shows a polymerase fold with jaws spread wide open. These data provide the first structural evidence that C-Pol2 contains a DNA polymerase fold³³ (Supplementary Movie 2). In agreement with the notion that certain elements are only flexibly tethered to the delta-cat core, no density was retrieved for the N-terminal domain

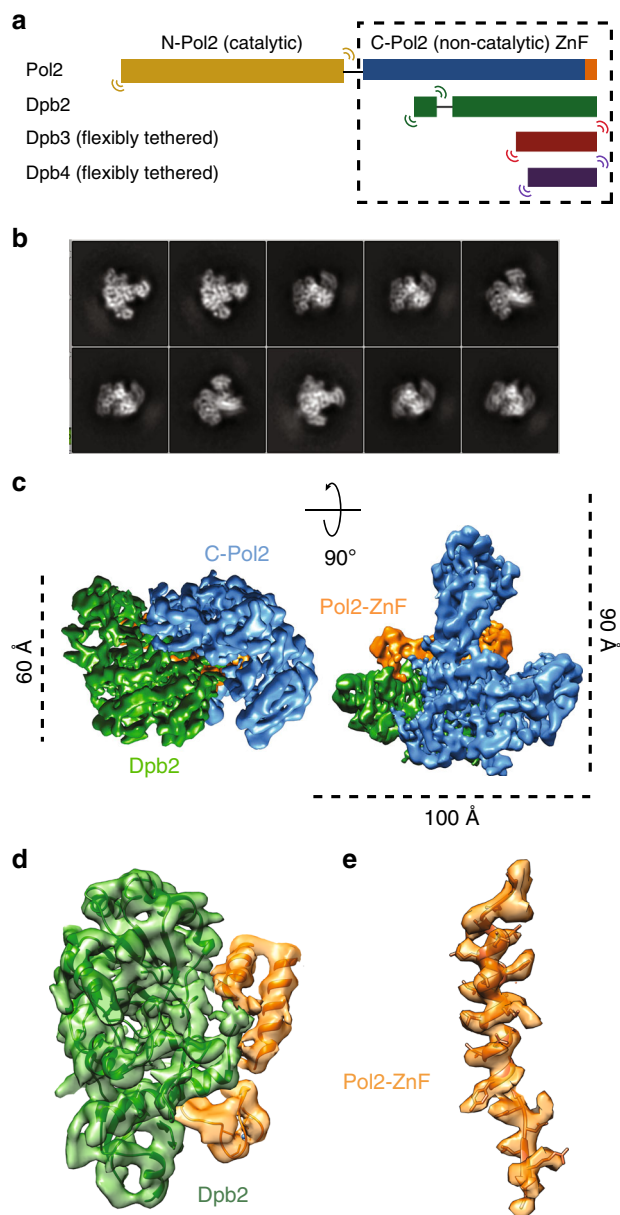


Fig. 1 Cryo-EM structure of the tetrameric Pol epsilon complex, lacking the catalytic domain (deltacat). **a** Subunit composition and domain organization of yeast Pol epsilon. N-Pol2 stands for N-terminal Pol2. C-Pol2 stands for C-terminal Pol2. ZnF stands for zinc-finger appendix. **b** 2D class averages of deltacat. **c** Surface rendering of the deltacat structure solved to 4.45 Å resolution. Dpb2 is green, Pol2 catalytically dead polymerase fold is blue, and Pol2 zinc-finger appendix is orange. **d** Atomic model for the yeast Dpb2 (green) bound to the Pol2 C-terminal zinc-finger appendix (orange), built into the cryo-EM map. **e** Detail of the Pol2 zinc-finger appendix (further map sharpening with phenix.auto_sharpen)

of Dpb2, nor for the histone-like subunits Dpb3-Dpb4. We speculated at this stage that at least one of these elements might become structured once Pol epsilon engages other replisome partner proteins (further discussed below). Our structure of the Dpb2/C-Pol2 interaction core explains key Pol epsilon phenotypes. For example, the C-terminus of Dpb2 intimately contacts C-Pol2, explaining why a truncation of the last six amino acids in Dpb2 prevents Dpb2 binding to Pol2-Dpb3-Dpb4 and results in a lethal phenotype⁴² (Fig. 2b). Likewise, a so-called ZnF1 element

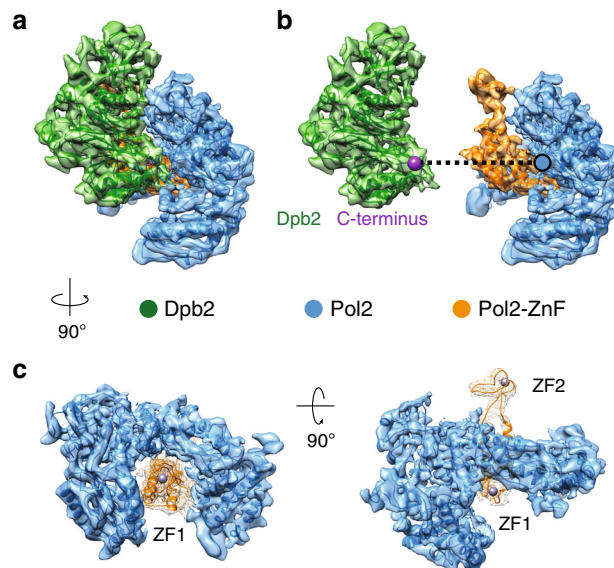


Fig. 2 Interaction between C-Pol2 and Dpb2. **a** Atomic model of C-Pol2 and Dpb2 built into the cryo-EM map. **b** Dpb2 C-terminus is poised towards the C-Pol2 interface, explaining why a truncation of the Dpb2 C-terminal region results in a lethal phenotype. **c** Pol2 zinc-finger appendix resides in the core of the Pol2 polymerase fold. This explains why a point mutation disrupting ZF1 is not compatible with viability. A second zinc-finger motif (ZF2) projects from the core of the complex

in the Pol2 zinc-finger appendix emerges as the organizing center of the deltacat core, explaining why cysteine-to-alanine single amino acid changes in this region can alter the essential non-catalytic Pol epsilon core, hence abolishing cellular growth (Fig. 2c)³⁵.

DNA binding by Pol epsilon. If C-Pol2 and Dpb2 are non-catalytic modules that evolved from DNA-processing enzymes⁴³, we reasoned that these domains might have retained their DNA-binding function. The DNA-binding domain of Pol alpha subunit Pol1 has been co-crystallized with DNA⁴¹. We therefore asked whether the open polymerase configuration found in C-Pol2 could still retain DNA-binding capabilities. Structure superposition revealed no obvious steric clashes between the open C-Pol2 polymerase fold and a primer-template junction. However, coulombic surface coloring indicates that the C-Pol2 polymerase domain lacks the positively charged region seen in DNA-binding grooves of other DNA polymerases. Furthermore, inspecting a more complete Pol2 structure that extends beyond the conserved polymerase module revealed that the C-terminal zinc-finger appendix occludes the DNA-binding groove in the dead polymerase fold (Fig. 3a–c). Admittedly, such tight polymerase–zinc-finger interaction might have been stabilized by the crosslinking agent used in our preparation. Likewise, this configuration might change in larger complexes such as full-length Pol epsilon or in a helicase–polymerase assembly (further addressed below). Nonetheless, the observations of an occluded DNA-binding site and the coulombic colored surface of the catalytically dead polymerase invite the prediction that C-Pol2 might have lost the ability to bind to DNA. To address this, we performed gel-shift assays to probe the DNA-binding function of various (non-cross-linked) Pol epsilon variants. As expected, DNA binding was observed for the wild-type, full-length tetrameric complex, and for the isolated full-length Pol2 polypeptide, which contains the DNA synthesis domain³². The deltacat construct, lacking the

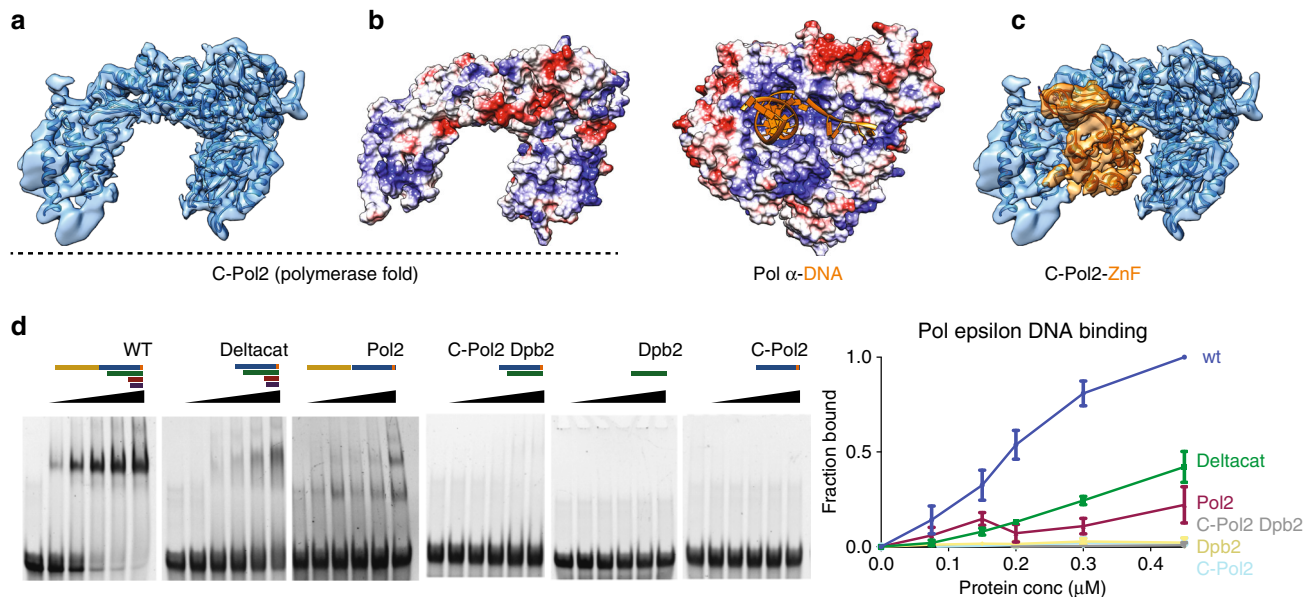


Fig. 3 The C-terminal half of Pol2 contains a catalytically dead polymerase fold that has lost its DNA-binding function. **a** C-Pol2 contains an inactive polymerase fold with jaws wide open. **b** Coulombic surface coloring of the C-Pol2 catalytically dead polymerase reveals a lack of positive charges in the vestiges of the DNA-binding groove, while the DNA-binding site in the related Pol alpha catalytic domain is positively charged. **c** The DNA-binding groove in C-Pol2 is occupied by the Pol2 zinc-finger appendix. **d** DNA-binding assay with various Pol epsilon variants. Only constructs containing the N-Pol2 catalytic domain or the histone-related proteins Dpb3-Dpb4 bind to DNA. We were unable to detect any DNA binding for C-Pol2 and Dpb2. On the right, quantification of the DNA-binding assays. Each experiment was repeated three times and error bars indicates standard deviation. Also refer to Supplementary Fig. 3

catalytic domain but containing ancillary subunits Dpb3-Dpb4, also resulted in clear gel retardation, in line with the notion that these histone-like proteins bind to DNA³¹. Importantly, no DNA binding was detected for C-Pol2, Dpb2 or a complex of the two (Fig. 3d and Supplementary Fig. 3). This observation is in line with the occluded DNA-binding site observed from the structure and indicates that the essential modules in the eukaryotic leading-strand polymerase are not DNA-binding factors.

Structure of CMG-Pol epsilon on a pre-formed DNA fork. To understand the function of the essential C-Pol2 and Dpb2 modules during replisome progression, we determined the structure of Pol epsilon associated with a fork-engaged CMG complex. To this end, we produced yeast CMG using a single yeast overexpression strain²⁸. We added a slowly hydrolysable nucleotide analog (ATPγS) to stabilize DNA binding by the MCM motor²³. Using these reagents, we immobilized the CMG on streptavidin-coated magnetic beads, bearing a desthiobiotin-labeled pre-formed DNA fork as bait. A full-length Pol epsilon variant containing inactivating mutations in the N-terminal Pol2 exonuclease was used to prevent DNA-fork degradation. Because desthiobiotin has reduced affinity for streptavidin compared to biotin, elution with biotin was highly efficient, yielding a nucleoprotein preparation suitable for single-particle cryo-EM analysis (Fig. 4a, b and Supplementary Fig. 4). To maximize particle numbers, we have absorbed our specimen using two subsequent applications, on lacey grids coated with an additional layer of ultrathin carbon. Particles were imaged on a Titan Krios EM with a K2 detector in counting mode. High-resolution 2D averages showed recognizable CMG assemblies with Pol epsilon decorating the ATPase tier of MCM, as previously reported in low-resolution negative-stain studies^{21,28} (Fig. 4c). Although end-on views of the MCM ring constituted the majority of particles,

side and tilted views were sufficiently represented to yield an isotropic structure (Supplementary Fig. 5). Three-dimensional reconstruction based on 78,556 particles yielded a structure with an average resolution of 4.9 Å and local resolution estimation revealed marked variations, ranging from 4.5 Å in the ATPase core of MCM to 7.5 Å on the Pol2 surface (Fig. 4d and Supplementary Fig. 5-6). This resolution is easily sufficient for a reliable docking of yeast CMG⁴⁴ and of the new atomic model of Pol epsilon deltacat (this study), both of which were built on higher-resolution cryo-EM maps. Whereas docking of yeast CMG required fitting of individual subdomains of the N-terminal and ATPase tiers as independent rigid bodies^{25,26,44}, deltacat could be docked into unoccupied density as one rigid body, resulting in an unambiguous fit (Fig. 4d and Supplementary Movie 3). Our observation indicates that deltacat maintains the same compacted configuration even when crosslinking agents are omitted from the preparation, when full-length Pol epsilon is used and when the polymerase is bound to CMG. Notably, in the cryo-EM map, the catalytic domain of Pol epsilon is invisible, as previously reported for non-crosslinked CMG-Pol epsilon preparations^{21,28}. Our structure shows that the CMG is stably interacting with the duplex/single-stranded DNA junction of the replication fork. Here, the double helix enters the MCM pore through the N-terminal tier, and single-stranded DNA (the leading-strand template) is captured by a set of ATPase pore loops (Mcm6-2-5-3, Fig. 5). As prereported in previous CMG-DNA-fork structures, the lagging strand template, excluded from the MCM ring, cannot be resolved in our structure⁴⁴. Furthermore, no obvious density for single-stranded DNA could be recognized bound to Pol2/Dpb2, confirming the notion that the essential catalytically inactive modules of Pol epsilon do not bind to DNA.

The observation of MCM interacting with the double helix in our ATPγS-CMG-Pol epsilon complex is noteworthy, given that previous studies on the CMG bound to a non-hydrolysable ATP

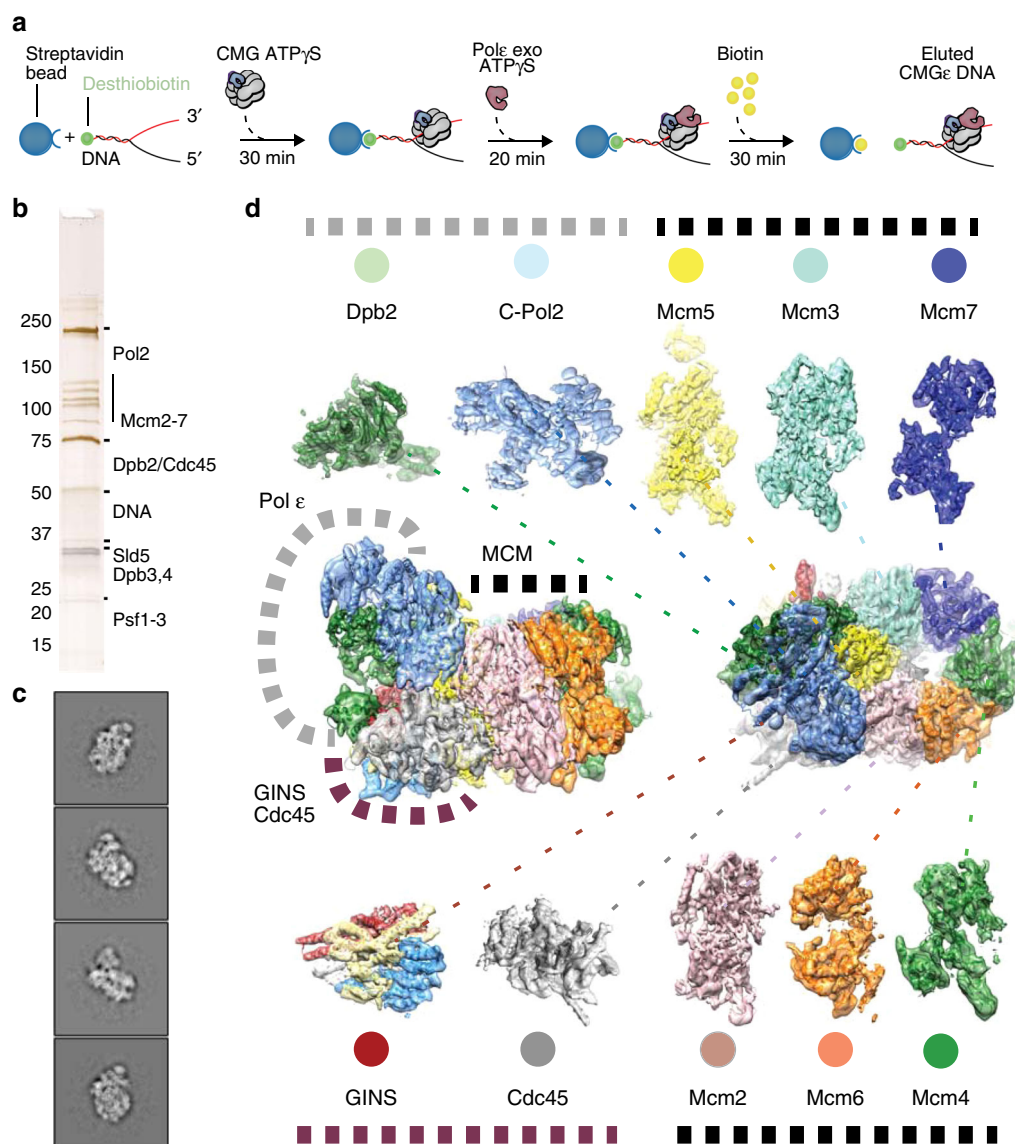


Fig. 4 Cryo-EM structure of CMG-Pol epsilon. **a** Diagram of the reconstitution of CMG-Pol epsilon on a pre-formed fork. CMG stands for Cdc45-MCM-GINS. **b** Silver-stained SDS-PAGE gel of the reconstituted CMG-Pol epsilon-DNA complex. **c** Two-dimensional class averages of the CMG-Pol epsilon-DNA complex. **d** Cryo-EM structure of CMG-Pol epsilon with docked/real-space refined homology models of CMG and C-Pol2/Dpb2 components

analog showed single-stranded DNA inside the ATPase ring but no visible duplex DNA^{25,44}. Productive engagement of the DNA duplex was instead previously captured only for a subset of translocating particles, in an ATP-CMG-fork preparation, halted by a DNA roadblock placed on duplex DNA⁴⁴. To explain the difference in CMG-fork nexus binding in the presence or absence of the polymerase, we hypothesized that Pol epsilon association with the ATPase tier of ATP γ S-CMG-DNA might cause a conformational change that promotes interaction with the DNA junction. Close inspection of the ATPase structure in ATP γ S-CMG-Pol epsilon-DNA indicates that polymerase association indeed alters the configuration of MCM active sites, causing compaction of the Mcm3-5-2 subunits (with the highest local resolution in the cryo-EM map centered around Mcm5, Fig. 5a) and relaxation of the neighboring ATPase interfaces. Concomitantly, the nucleotide occupancy state in the ATP hydrolysis centers changes, with density peaks compatible with ATP γ S detected in the Mcm5-3 and Mcm2-5 ATPase sites, while all other sites appeared nucleotide-free (Fig. 5b). This occupancy

pattern differs from that of ATP γ S-CMG-DNA or ATP-CMG-DNA-roadblock, where the Mcm6-2 interface is nucleotide-engaged, alongside Mcm5-3 and Mcm2-5⁴⁴. This change in the ATPase structure likely alters DNA engagement and might be the reason why fork nexus binding can be observed in our ATP γ S-bound CMG-Pol epsilon structure (Fig. 5c). Morphing between the ATP-CMG-DNA-roadblock and ATP γ S-CMG-DNA-Pol epsilon structures show structural changes in the two states appear to promote a slight rotation of the double helix as DNA advances towards the MCM central channel (Supplementary Movie 4). This observation starts to provide insights into how changes in the ATPase state might promote helicase movement along the DNA^{23,45–47}.

Analysis of CMG-Pol epsilon contacts. Close inspection of the cryo-EM map after docking of the CMG and deltat structures highlighted unoccupied density. One region departs from the N-terminus of CTD-Dpb2 and projects as an extended arm towards GINS (Fig. 6a). Although the local resolution in this region of the

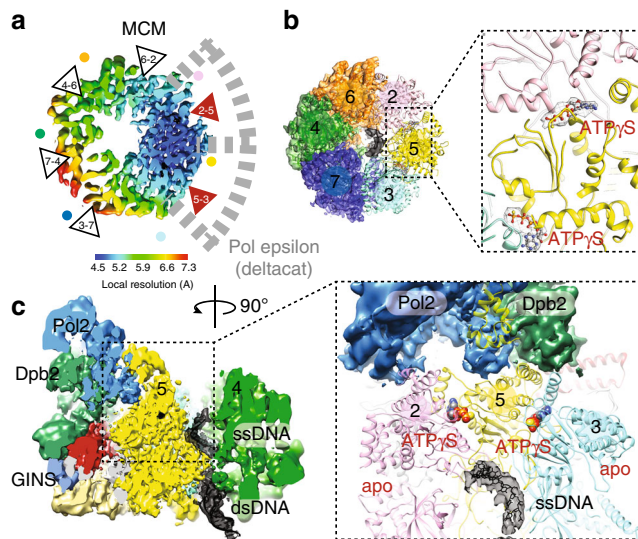


Fig. 5 ATPase state and DNA binding in the CMG-Pol epsilon complex. **a** Inspection of the local resolution map indicates that the ATPase site clamped by C-Pol2/Dpb2 is highly stable, with the Mcm5 AAA+ module reaching resolutions as high as 4.5 Å. **b** Single-stranded DNA is captured by ATPase pore loops of Mcm3, -5, -2, and -6. ATPγS is bound to the Mcm5-3 and Mcm2-5 subunits. **c** A cut-through view of the CMG-Pol epsilon reveals duplex DNA entering through the N-terminal domain of MCM and the leading-strand template captured within the ATPase domain. A 90° rotated view of the Mcm3-5-2 region reveals how C-Pol2/Dpb2 clamping stabilizes nucleotide binding and single-stranded DNA engagement by Mcm2, Mcm5 and Mcm3 pore loops

map is relatively low (i.e., 6.5–7.5 Å resolution, as seen in Supplementary Fig. 5), an accurate fit can be obtained from docking of N-terminal Dpb2, generated by homology modeling based on the nuclear magnetic resonance structure of the human ortholog³⁷. The resolution in this region is not sufficient to see any of the amino acid side chains involved in the GINS contact; however, inspection of our docking result provides confidence in the overall architecture of our model, given that the C-terminus of NTD-Dpb2 points towards the N-terminus of the CTD-Dpb2 module described above (Fig. 6a). The two domains appear tethered by a flexible linker, explaining why NTD-Dpb2 becomes visible only when stabilized by partner-protein interactions. In fact, inspection of the CMG contacts reveals that N-terminal Dpb2 engages C-terminal Psf1, in agreement with biochemical studies on Pol epsilon replisome incorporation by the Labib group (Fig. 6a)³⁰. A second contact point involves the C-terminal winged helix (WH) appendix of Mcm5, which is clamped between the inactive polymerase and zinc-finger modules of Pol2 (Fig. 6c). All docked structures were subjected to real-space refinement using a combination of Coot⁴⁸ and Phenix⁴⁹.

Notably, in previous MCM-containing structures, the Mcm5 WH domain can be found occluding the MCM central channel when the ATPase motor is not DNA engaged^{26,50,51}. We speculate that, by pulling the Mcm5 WH domain away from the central channel, Pol2-Dpb2 might promote productive DNA engagement inside the MCM pore. This is in agreement with the observation that ATPγS-CMG-Pol epsilon intimately engages the double helix at the DNA fork, as described above (Fig. 5c). Other CMG-Pol epsilon contacts can be visualized between C-Pol2/Dpb2 and the MCM AAA+ tier. For example, Pol2 keeps the Mcm2-5 ATPase gate shut, with the dead polymerase module

touching Mcm5 and the zinc-finger appendix touching Mcm2. In particular, the ZnF2 element mapping in the Pol2 C-terminus contacts the Mcm2 ATPase, explaining a temperature-sensitive phenotype for cysteine-to-alanine substitutions in this peripheral element³⁵. Likewise, the Dpb2 core sits across the Mcm5-3 ATPase interface (Fig. 6c). A structural role of Pol2 and Dpb2, clamping Mcm2-5-3 ATPase domains close together, agrees with our observation that the active sites at the Mcm2-5 and Mcm5-3 interfaces are ATPγS occupied, while other ATPase sites in the MCM ring are empty (Fig. 5a–c).

We note that the role of the C-Pol2/Dpb2 elements contacting MCM appears to match the function of GINS/Cdc45 in the CMG, although the two pairs of factors act on opposed tiers of the helicase ring^{24–26}. In fact, GINS/Cdc45 latch across the Mcm2-5 gate and stabilize the Mcm5-3 interface by engaging the N-terminal collar^{24–26}, while C-Pol2/Dpb2 are poised to stabilize the Mcm2-5/5-3 AAA+ interfaces (i.e., the sites essential for DNA unwinding²³). Our new helicase-polymerase structure contains the pre-formed CMG bound to Pol epsilon on a model fork substrate and informs us on the architecture of the activated helicase poised to unwind the replication fork. We postulate that interactions seen in our structure might be also important for replication initiation. Two notions are key in this context. First, GINS and Pol epsilon are known to be recruited onto the MCM during the same step towards origin activation¹⁹. Second, stable CMG formation requires release of ADP and binding of ATP². Our finding that Pol2 and Dpb2 directly contact three key ATPase domains of MCM suggests a mechanism by which this nucleotide exchange might be modulated.

The role of C-Pol2 and Dpb2 in CMG formation. Our structure of delcat Pol epsilon reveals an extensive interaction interface between C-Pol2 and Dpb2 (Fig. 2a). Furthermore, our structure of the CMG-Pol epsilon complex, reconstituted on the fork using recombinant active helicase and polymerase, establishes that Dpb2 mainly interacts with GINS (Fig. 6a) and C-Pol2 mainly contacts the MCMs (Fig. 6b). Given these observations, we asked whether elements of our CMG-Pol epsilon structure on the DNA fork would be retained during the process of Pol epsilon-dependent CMG assembly, on path to origin firing. We postulated that GINS recruitment and CMG formation might only occur when both Dpb2 and C-Pol2 are present in the same complex, as the physical link between GINS and MCM would be preserved. To test this hypothesis, we used a yeast replication system reconstituted with purified proteins¹³ to establish the minimal complement of Pol epsilon domains that are required to make stable CMG. To this end, we loaded MCM double hexamers onto an immobilized DNA fragment and added a full complement of firing factors to promote the assembly of a stable CMG complex^{2,13}. As shown in Fig. 6d, when wild-type Pol epsilon was substituted for delcat, CMG was still assembled, although less efficiently. A Pol epsilon variant containing both C-Pol2 and Dpb2 showed the same efficiency of CMG formation as delcat, indicating that ancillary subunits Dpb3/Dpb4 are not required for CMG assembly. As we predicted, the isolated full-length Pol2, C-Pol2, or Dpb2 subunits were unable to support CMG formation (Fig. 6d). We then tested whether the CMG assembled by these Pol epsilon variants could support DNA replication, by additionally including the proteins required for complete leading and lagging-strand synthesis⁵². Only wild-type Pol epsilon, delcat, and C-Pol2/Dpb2 supported DNA replication (Fig. 6e). As previously reported, DNA replication products in the presence of delcat were shorter compared to wild-type Pol epsilon,

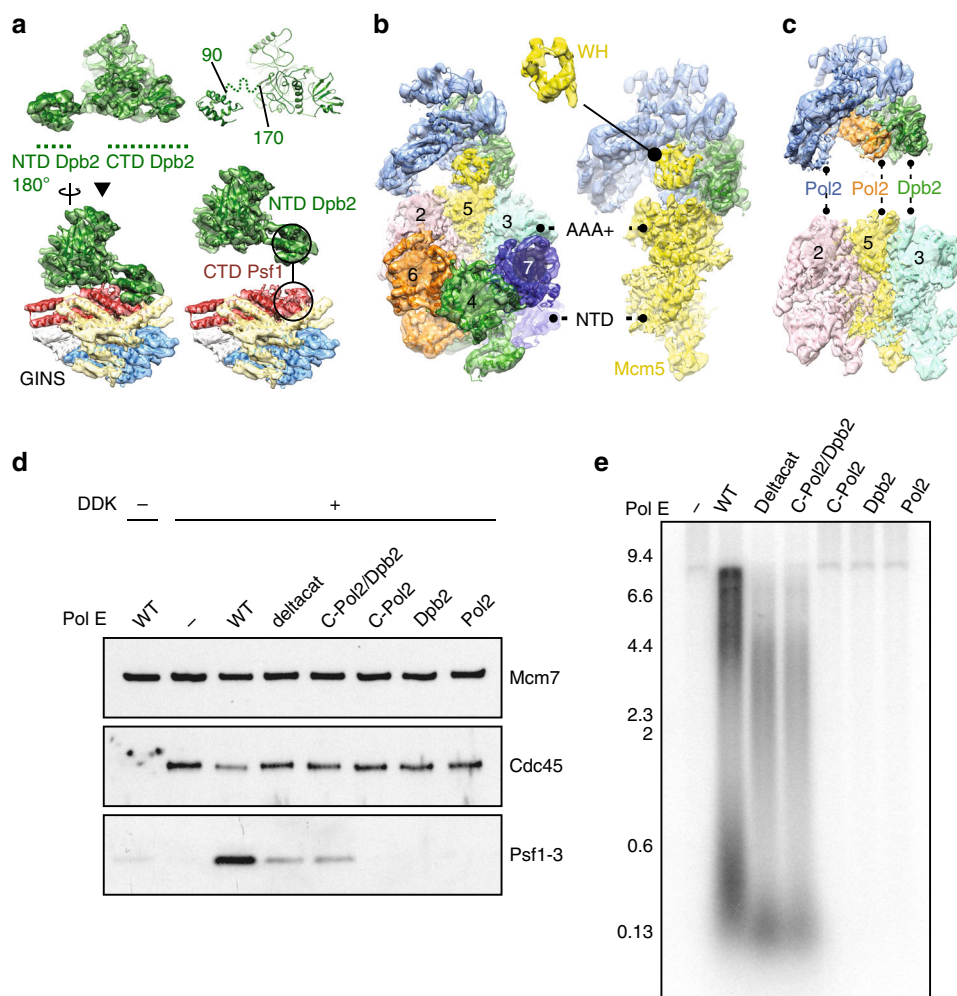


Fig. 6 Interactions between Pol epsilon and the CMG. **a** A model for full-length Dpb2. N-terminal and C-terminal domains are tethered by a flexible linker. N-terminal Dpb2 contacts the C-terminal domain of GINS subunit Psf1. **b** The winged helix domain of Mcm5 is clamped between the catalytically dead polymerase in Pol2 and the zinc-finger appendix. **c** C-Pol2 and Dpb2 keep the ATPase domains of Mcm2-5-3 in a compacted state. C-Pol2 interacts with Mcm2 (via the polymerase fold) and Mcm5 (via the ZF2 element in the zinc-finger appendix, also see Fig. 2c). Dpb2 contacts the Mcm3 ATPase domain. **d** A complex containing both C-Pol2 and Dpb2 represents the minimal complement of Pol epsilon modules required for assembly of the CMG. **e** A complex of C-Pol2/Dpb2 but not the two isolated protomers support DNA replication in vitro

consistent with the idea that in the absence of the Pol2 catalytic domain, leading-strand synthesis by *trans*-acting Pol delta occurs at a slower rate⁵². Importantly, in reactions containing C-Pol2/Dpb2, we observed the same amount and profile of replication products as with deltatcat. This is in agreement with the notion that the remaining Dpb3 and Dpb4 subunits do not play a direct role in the DNA replication reaction, but rather modulate histone redeposition at the replication fork^{53,54}. As expected from their defect in CMG assembly, the isolated Pol2, C-Pol2, and Dpb2 subunits failed to support DNA replication in this system (Fig. 6d–e). Altogether, our results are compatible with the idea that C-Pol2 and Dpb2 must act as a heterodimeric complex, to link GINS to the MCM during CMG establishment. Cryo-EM characterization of the complete CMG assembly reaction (including CDK, DDK, Sld2, Sld3/7, and Dpb11) will be key to understanding the essential structural role of C-Pol2/Dpb2 during replication initiation.

Analysis of CMG productively bound to the replication fork. During replisome progression, it is unknown whether C-Pol2 and

Dpb2 indeed remain anchored to the ATPase domain of the advancing CMG. To address this issue, we reconstituted CMG formation and Mcm10-dependent DNA unwinding using the in vitro system with purified yeast proteins¹³. Briefly, origin activation reactions were assembled on linear, biotinylated DNA tethered to streptavidin-coated magnetic beads. The linear DNA fragment was blocked at the two ends with covalent protein–DNA roadblocks to prevent linear diffusion of MCM off the DNA. This substrate was used to load multiple MCM double hexamers and firing factors were added to promote origin activation. Subsequently, elution from the streptavidin beads was achieved by DNA digestion at a single site, leaving the doubly blocked DNA segment intact. Using 2D classification of negatively stained data, we observed that only a subset of these double hexamers were converted to CMG, causing inactive MCM double hexamers to be pushed along duplex DNA in front of the helicase and against the protein–DNA roadblock² (Fig. 7a). This resulted in the formation of stacks of MCM particles (trains), which are capped at one end by a CMG engine (Fig. 7b–d). We can exclude the possibility that trains are the mere product of protein

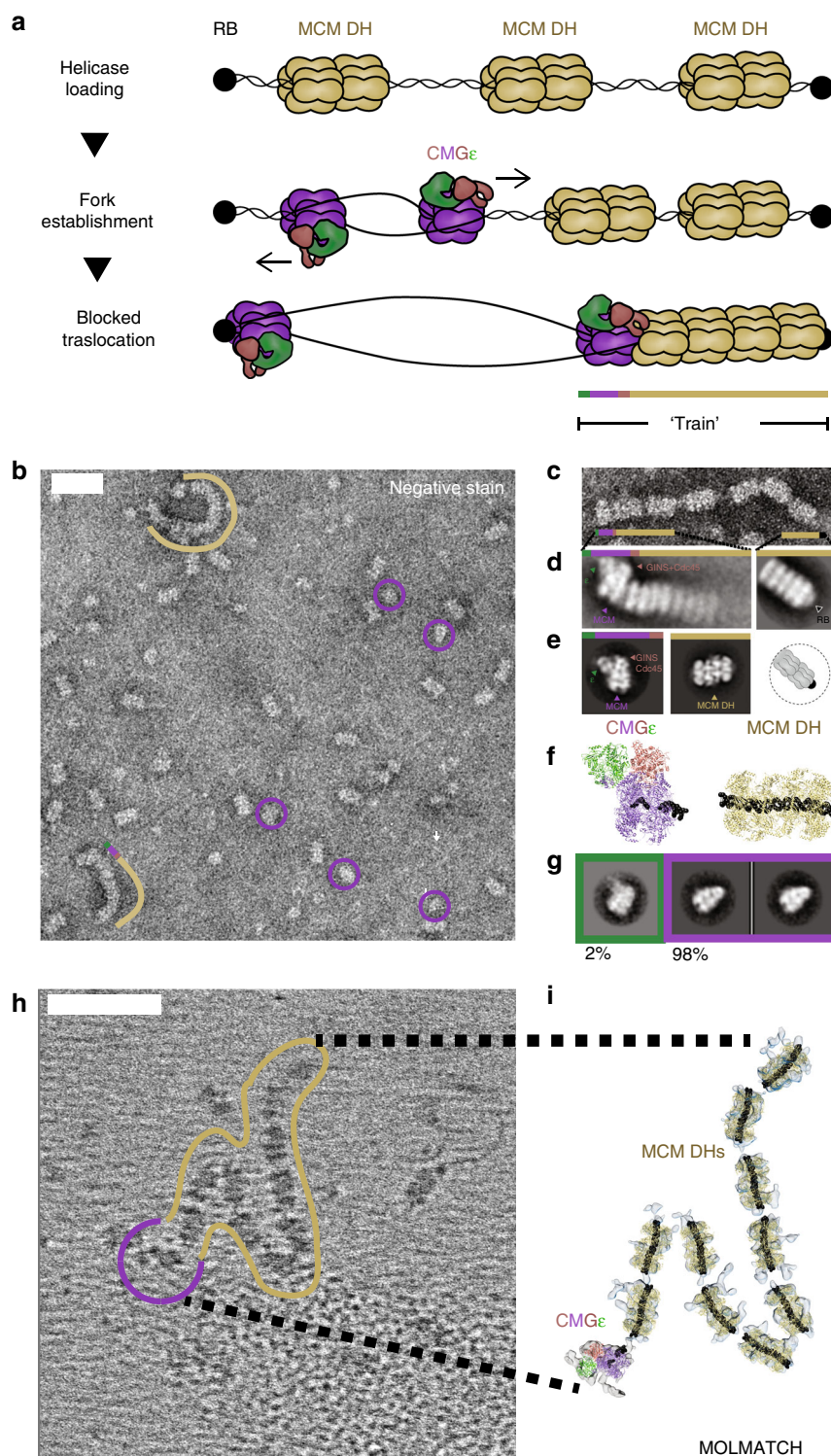


Fig. 7 Composition of the replicative helicase productively engaged to the replication fork. **a** Diagram of the EM-based translocation assay. Multiple MCM double hexamers are loaded onto a linear stretch of duplex DNA capped with protein-DNA roadblocks. Only certain MCM double hexamers are activated and translocating CMGs push MCM double hexamers against the DNA roadblock. **b** Representative negative-stain micrograph reveals accumulation of MCM trains (marked with a khaki line) alongside isolated CMGs (marked with purple circles). Scale bar 50 nm. **c** Detail of a negative-stain micrograph revealing that MCM trains are made of stacked double hexamers loaded onto DNA. **d** Two-dimensional averages of the CMG capping the trains and opposed end of trains capped by a protein roadblock. Most MCM-pushing CMG particles are bound to Pol epsilon. **e** 2D averages of CMG-Pol epsilon and MCM double hexamers, next to a cartoon of an MCM blocked by a protein-DNA roadblock. **f** Atomic structures of CMG-Pol epsilon and MCM double hexamer, both bound to DNA. **g** 2D class averages of isolated CMGs observed in the MCM train experiment. Most CMGs that failed to translocate up to the roadblock are not engaged by Pol epsilon. **h** Cryo-electron tomogram of an MCM train. Scale bar 50 nm. **i** MCM and CMG structures placed into the cryo-electron tomogram using template matching approaches. This experiment supports the notion that CMG-Pol epsilon particles push MCM double hexamers against a protein-DNA roadblock to form MCM trains

aggregation, because they disappear when covalent protein roadblocks are omitted, or when the Mcm10 firing factor is excluded from the origin activation reaction (Supplementary Fig. 7)². To define the identity of the helicase productively engaged to the DNA fork, we first analyzed MCM-containing particles that were not train incorporated. These particles fell in two categories: isolated MCM double hexamers and CMGs (Fig. 7e–g). Remarkably, isolated CMGs were largely polymerase free, with only a small fraction (2% of recognizable, averaged particles) of the helicase bound by Pol epsilon (Fig. 7g). To establish the composition of the active CMG productively bound to the DNA fork, we then focused our analysis on the tips of the MCM trains. We confirmed that one end of the train was capped by the protein roadblock found in direct contact with an MCM double hexamer (Fig. 7e). At the opposed end of the train, the vast majority of CMGs (75–100% of recognizable, averaged particles in different repeats of the same experiment) were bound by a AAA+ interacting Pol epsilon complex (Fig. 7d). Our observation was further supported by cryo-electron tomographic analysis (Fig. 7h). In this experiment, we used a template matching approach (as implemented in MOLMATCH⁵⁵) to recognize MCM double hexamers and CMG particles in the MCM trains. As predicted from our negative-stain experiment, we found high correlation peaks for MCM double hexamers along the length of the train and one CMG particle capping one end of the train. We also observed that a Pol epsilon-bound form of CMG best matches the cryo-tomographic density in this region (Fig. 7i, Supplementary Fig. 7, and Supplementary Movie 5).

In summary, these data indicate that the translocating form of the CMG is Pol epsilon bound. Combined with our cryo-EM reconstruction of the fork-bound CMG-Pol epsilon, our results suggest that tight Pol epsilon binding to the AAA+ tier of the MCM ring might stabilize productive helicase engagement to the duplex/single-stranded DNA junction.

Discussion

In this study, we have provided the first structural evidence that the catalytic subunit Pol2 contains a tandem repeat of polymerase modules³³ (Figs. 1a, 2a–c). In Pol2, the N-terminal repeat contains the DNA synthesis function³², while the C-terminal repeat is catalytically inactive³⁵. We showed that C-Pol2 shares an extended interface with the Pol epsilon subunit Dpb2, which in turn contains a catalytically dead exonuclease³⁴ (Figs. 1d, 2a,b). Having evolved from two DNA-processing enzymes, not only have C-Pol2 and Dpb2 lost their catalytic activity⁴³ but also their DNA-binding functions. In fact, we found that only Pol epsilon permutations that contain the N-Pol2 catalytic module³² or histone-like factors Dpb3-Dpb4³¹ can bind to DNA, as observed in gel-shift assays. Conversely, no DNA association could be observed for C-Pol2 or Dpb2 (Fig. 3d).

Our cryo-EM structure of an isolated Pol epsilon deltatcat derivative explains why C-Pol2 cannot bind to DNA. In particular, the inner surface in the polymerase fold is not as positively charged as the DNA-binding groove of other replicative polymerases such as Pol alpha^{41,43}, and it is further occluded by the C-terminal zinc-finger appendix of Pol2 (Fig. 3a–c). In line with these observations, our cryo-EM structure of the DNA-engaged CMG-Pol epsilon showed DNA binding by MCM proteins, but not by C-Pol2 and Dpb2 (Fig. 5c; while, due to flexibility, N-Pol2 and Dpb3-Dpb4 were not visible). Given that these are not enzymes nor DNA-binding factors, we reasoned that C-Pol2 and Dpb2 must play a structural role in the replisome. This scenario is reminiscent of Cdc45 that has evolved from a RecJ exonuclease⁵⁶. Cdc45 has lost its DNA-processing functions, while it has acquired a key structural role in reconfiguring the MCM motor,

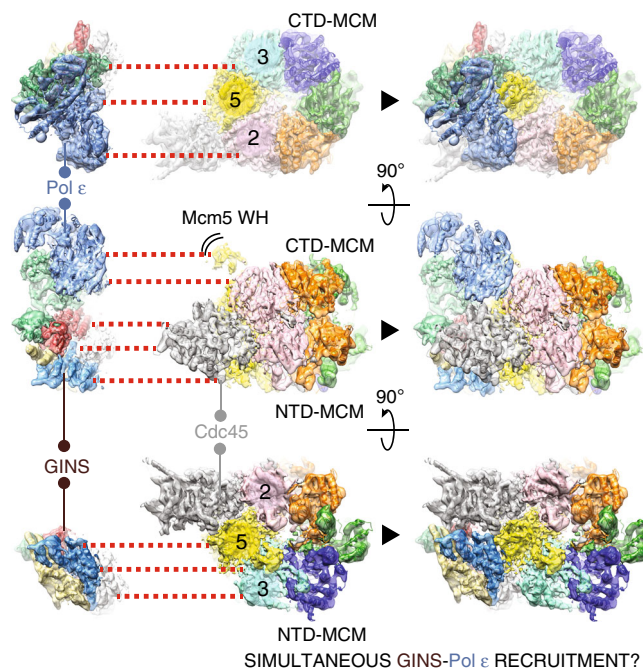


Fig. 8 Proposed mechanism for the concomitant recruitment of GINS and Pol epsilon onto MCM. By interacting with Cdc45 on the N-terminal MCM face, GINS stabilizes the Mcm2-5-3 N-terminal interactions. C-Pol2 and Dpb2 in the Pol epsilon complex play a similar role, by stabilizing the Mcm2-5-3 AAA+ ATPase interactions. Given that GINS and Pol epsilon are recruited onto MCM as part of the same complex, concomitant binding of both factors might promote activating conformational changes in the helicase, eventually leading to origin activation

to promote DNA melting and fork unwinding within the CMG^{23,24}.

In support of a structural role for Dpb2 and C-Pol2, inspection of the DNA fork-CMG-Pol epsilon structure reveals that these two modules provide a molecular bridge across CMG components, with Dpb2 mainly contacting GINS, and C-Pol2 contacting MCM (Fig. 6a–b). GINS and Pol epsilon are recruited onto MCM-Cdc45 as part of the same pre-loading complex¹⁹. Previous work on the CMG structure established that GINS and Cdc45 bind to the N-terminal tier of Mcm2-5-3, stabilizing a planar configuration of the MCM ring and locking a natural gate, between MCM subunits 2 and 5^{24–26,57,58}. In the CMG-Pol epsilon structure, we now found that C-Pol2/Dpb2 interact with the same Mcm2-5-3 protomers, poised to stabilize the C-terminal AAA+ interfaces. Our observation is noteworthy, given that Mcm2-5 and Mcm5-3 contain the two ATPase centers that are essential for CMG function²³, and suggests a mechanism for the simultaneous recruitment of GINS and Pol epsilon (Fig. 8).

A direct contact between GINS/Pol epsilon and MCM might play a role both during origin activation as well as replication fork advancement. To test the idea of a role during activation, we have used *in vitro* reconstitution of DNA replication^{2,13}, to show that a combination of C-Pol2 and Dpb2, but neither of the two factors in isolation, constitute the minimal complement of Pol epsilon modules required for CMG formation (Fig. 6d–e). Therefore, key aspects of the CMG-Pol epsilon architecture described in our cryo-EM map appear to be important for origin activation^{35,43}.

Our structural studies also provide insights into replication fork progression. In comparing our new DNA-CMG-Pol epsilon structure to the published DNA-CMG structure (PDB entry 5U8S)⁴⁴, we found that C-Pol2/Dpb2 association with the C-

terminal face of MCM alters the ATPase conformation by stabilizing the Mcm5-ATPγS-Mcm3 and Mcm2-ATPγS-Mcm5 interactions, while all other active sites are nucleotide-free (Fig. 5a–b). In these conditions, and for the first time in an ATPγS-CMG complex, the duplex/single-stranded DNA junction, and not just single-stranded DNA, can be seen engaged by the MCM complex. This feature is shared by all particles that contribute to high-resolution 3D structures in our dataset (Fig. 5c). Strikingly, fork nexus engagement was previously only observed when the helicase was incubated with ATP to promote DNA translocation and only in a small subset of helicase particles⁴⁴. Together with our EM observation that the translocating form of the CMG is Pol epsilon bound (Fig. 7), our data support the notion that polymerase binding promotes productive DNA fork engagement by the CMG.

Furthermore, our structure informs a model for helicase translocation at the replication fork. Previous structural reports on the *Drosophila* and yeast CMG helicase, from us²⁵, the Berger/Botchan²⁴, and from the O'Donnell/Li²⁶ laboratories, showed that the Mcm2-5 interface is highly dynamic and that ATP binding can shift the equilibrium from a relaxed (nucleotide-free) to a tight (nucleotide-bound) state of the ATPase side of the MCM ring in the CMG. This observation led to us and others suggest that DNA translocation could occur with the helicase “inchworming” along DNA through relaxing and tightening of the Mcm2-5 AAA+ interface (referred to as “pump-jack model” in the yeast study)^{25,26}. Alternatively, DNA translocation would occur via a distinct mechanism that still needs to be determined, while the relaxed Mcm2-5 AAA+ structure in the CMG could represent a pausing state of the helicase²⁵. Our new structural data appear to support the latter model, as Pol epsilon engagement by the CMG seems incompatible with the conformational rearrangements described in the pump-jack helicase^{8,26}. The three structural changes described in the pump-jack model involve opening of a gap between Mcm2 and Mcm5, transition from a planar to a spiral ATPase tier and movement of the Mcm5 WH domain. These three conformational switches would seemingly all contribute to disrupting the multipartite Pol epsilon-binding site on the CMG (Supplementary Movie 6). In this study, we also provide evidence for Pol epsilon association occurring when CMG particles are productively fork engaged. This is why we now favor a model whereby a wide Mcm2-5 ATPase opening, which is incompatible with Pol epsilon binding, would cause helicase stalling (proposed before by Botchan and Berger⁵⁹), not DNA translocation. Alternatively, engagement between CMG and delta cat could be much more dynamic than we would predict by inspecting our structure. Future studies are needed to understand the relation between ATP binding/hydrolysis, helicase movement, and replicative polymerase exchange rates in the advancing replisome. The key to understanding replisome progression, we predict, will likely be fork stabilization factors Mrc1/Csm3/Tof1, which all contribute to achieving cellular rates in DNA replication reactions reconstituted in vitro⁵².

Methods

Yeast expression strains. Strains are based on W303. See Supplementary Table 1 for a list of all strains and genotypes used in this study.

Protein expression and purification. For expression of wild-type Pol epsilon and dropout variants, cells were grown in YEP media supplemented with 2% raffinose. Cells were arrested in the G1 phase at a density of $\sim 2\text{--}3 \times 10^7$ cells/ml with 100 ng/ml alpha factor for 3 h at 30 °C. Protein expression was then induced by adding galactose to 2% and growth continued for 3 h at 30 °C. Cells were harvested by centrifugation at 4000 rpm for 30 min in a Beckman Coulter J6-MC Centrifuge (Beckman JS-4.2 rotor) and washed with Buffer E (25 mM HEPES, pH 7.6, 10% glycerol, 1 mM dithiothreitol (DTT)) supplemented with 500 mM KOAc (Buffer E-500). Cells were spun down again in a Beckman Coulter Allegra® X-15R Centrifuge

and resuspended with Buffer E-500 (at half the pellet volume) and frozen dropwise into liquid nitrogen. Frozen droplets were crushed in a 6875D Freezer/Mill® Dual Chamber Cryogenic Grinder/Freezer mill (SPEX SamplePrep) using six cycles, intensity 15 (Precool 1 min, run 2 min, break 1 min), operating at -80°C . Cell powder was resuspended in Buffer E supplemented with complete protease inhibitor tablets (Roche).

Pol epsilon and dropout variants were prepared as follows: the powder was resuspended with 250 ml Buffer E supplemented with 400 mM KOAc (Buffer E-400) and protease inhibitors (Roche). Lysate was cleared by ultracentrifugation at 45,000 rpm for 1 h at 4 °C (Ti45 rotor, Beckman Coulter Optima L-100 XP Ultracentrifuge). For all proteins expressing a CBP tag (wild type, exo^- , and delta cat), 3 ml calmodulin beads (GE Healthcare) were pre-equilibrated in Buffer E-400, added to the cleared lysate, and supplemented with 2 mM CaCl_2 . For the remaining proteins (C-Pol2, C-Pol2/Dpb2, Dpb2, Pol2), 4 ml anti-Flag M2 affinity resin was pre-equilibrated in Buffer E-400 and added to the cleared lysate. All incubations occurred at 4 °C with end over rotation for 2 h. Flow-through was collected and beads were washed with 100 column volumes of Buffer E-400 (supplemented with 2 mM CaCl_2 for the CBP-tagged proteins). Proteins were eluted either using elution Buffer E-400 supplemented with 2 mM EGTA and 2 mM EDTA (CBP tagged proteins) or with Buffer E-400 supplemented with 1 mg/ml FLAG peptide (FLAG-tagged proteins). The elutions were pooled and injected into SP Sepharose Fast Flow 1 ml column (GE Healthcare) attached to a Mono Q 5/50 GL 1 ml column (GE Healthcare) in an Äkta purifier (GE Healthcare). Proteins were washed with either 20 CV Buffer E-300 (for all variants except exo^-) or Buffer E-400 (exo^-). Proteins were eluted after removal of SP Sepharose Fast Flow column over a 15 CV gradient (Buffer E 300–1500 mM KOAc for all variants apart from exo^- , where a 400–1000 mM KOAc gradient was used). The purest fractions were pooled either dialyzed or buffer exchanged to Buffer E-400 via gel filtration using a Superdex 200 Increase 3.2/300 column for cryo-EM or Superdex 200 10/300 GL for DNA-binding assays.

CMG purification was performed as follows: yJCZ3 was used to express CMG²⁸. Induction was performed using 2% galactose for 3 h at 30 °C, frozen dropwise in liquid nitrogen, and ground as described above. Cell powder was resuspended in buffer C (25 mM HEPES, pH 7.6, 0.02% Tween-20, 10% glycerol, 1 mM EDTA, 1 mM EGTA) supplemented with 15 mM KCl, 2 mM MgCl_2 , 2 mM β -mercaptoethanol, and complete protease inhibitors mixture. KCl was then added to 100 mM, and the lysate cleared by centrifugation. The clear lysate was incubated with anti-Flag M2 affinity resin at 4 °C, washed with C-100 buffer (buffer C with 100 mM KCl and 1 mM DTT), and eluted with C-100 buffer supplemented with 0.5 mg/ml FLAG peptide and complete protease inhibitors mixture. Peak fractions were pooled and loaded onto a HiTrap SP FF (GE Healthcare). The flow-through was collected and loaded onto a Mono Q 5/50 GL (GE Healthcare), washed with C-100 buffer, and eluted over 100 mM to 550 mM KCl gradient in C-100 buffer supplemented with 1 mM DTT. Peak fractions were pooled, diluted to 150 mM KCl in buffer C, loaded onto Mono Q 1.6/5 PC in buffer D (25 mM HEPES, pH 7.6, 1 mM EDTA, 1 mM EGTA, 1 mM DTT) supplemented with 150 mM KCl, and eluted over 150 mM to 550 mM KCl gradient in buffer D.

DNA sequences. All oligonucleotides were purchased from integrated DNA technologies (IDT). Oligonucleotides used for electrophoretic mobility shift assays were:

160 nt forward,
5'-ACCGATGTGGTAGGAAGTGAGAATTGGAGAGTGTGTTTTTTTTTTT
TTTTTTTTTTTTTTTTTTTTTTTTTTTGGAGAAAGAATGTGGTGAGGG
TTGGGAAGTGAAGGATGGGCTCGAGAGGTTTTTTTTTTTTTTTTTTTT
TTTTTTTTTTTTTT-3'

37 nt reverse,
5'-CCACTCCCAACCCTTCACCTTCCTACCCGAGCTCTCC-3'.

Oligonucleotides used for fork DNA affinity purification of CMG-Pol epsilon were:

leading-strand template,
5'/5deSBioTEG/
GCAGCCacgtGGCCGTTTTACAACGTCGTGACTGGGCACCTTGATCGGCCA
ACCTT-3'
lagging-strand template,
5'-GGCAGGCAGGCAGGCAGGCAGGCCGTGCGCGTGGTTCGTGCGGTTG
GCCGATCAAGTGCCGACGTACGACGTTGTAACGCGCCAGCGTGCGTG
C-3'

To anneal the DNA, the two oligonucleotides were mixed in an equimolar ratio and left to incubate at 95 °C for 3 min followed by slow cooling to room temperature.

Electrophoretic mobility shift assays. Purified wild-type Pol epsilon and dropout variants were pre-mixed in a dilution series (75, 150, 200, 300, and 450 nM) with DNA at a concentration of 300 nM, in a reaction buffer containing 25 mM HEPES, pH 8.0, 30% glycerol, 2 mM EDTA, 0.2 mg/ml bovine serum albumin (BSA), and 0.02% Triton-X. Binding was performed for 30 min at 4 °C. polyacrylamide gel electrophoresis (PAGE) made with 4% polyacrylamide, 3% glycerol, and 0.5× TAE polymerase was pre-run at 100 V for 1 h (4 °C).

Protein–DNA complexes were resolved by running the PAGE at 100 V for ~2 h (4 °C) in 0.5× TAE. Visualization of the complexes were done by staining the PAGE with Diamond Nucleic acid dye (Promega) for 15 min. Imaging was done with 1.5 s manual exposure using Bio-Rad Gel DOC XR+ equipped with the Bio-Rad image lab software.

Reconstitution of CMG Pol epsilon bound to a pre-formed fork. To reconstitute CMG-Pol epsilon on DNA, a bead affinity approach was used. Seven microliters of M-280 Streptavidin Dynabeads™ (Thermo Fisher) slurry was added to low-binding microcentrifuge tubes and all incubations occurred at 30 °C with 1250 rpm shaking in a thermomixer. Beads were washed twice with 20 µl DNA-binding buffer (25 mM HEPES 7.6, 1 M NaCl, 10% glycerol, 0.01% NP-40, 1 mM EDTA). Twenty microliters of 250 nM fork DNA was added and then incubated for 30 min. The supernatant was collected and the beads were washed once with 20 µl DNA-binding buffer and once with 20 µl protein-binding buffer (25 mM HEPES 7.6, 100 mM KOAc, 10 mM Mg(OAc)₂, 10% glycerol, 0.01% NP-40, 1 mM DTT, 2 mM ATPγS). Twenty microliters of 250 nM CMG was added and the reaction was incubated for 30 min. The supernatant containing unbound CMG was collected and beads were washed once with 20 µl protein-binding buffer. Twenty microliters of 80 nM polymerase epsilon exo[−] was added to the beads and then incubated for 20 min at 30 °C and 1250 rpm. Beads were washed once with 20 µl protein-binding buffer and once with 20 µl protein-binding buffer without glycerol. Complexes were eluted by the addition of 10 µl elution buffer (25 mM HEPES 7.6, 100 mM KOAc, 10 mM Mg(OAc)₂, 0.01% NP-40, 1 mM DTT, 2 mM ATPγS, 400 nM biotin) and then incubated for 30 min. Elutions were pooled and used for cryo-EM grid preparation.

Cryo-EM grid preparation. Deltacat polymerase epsilon grids were prepared as follows: purified deltacat polymerase epsilon was first crosslinked with 0.01% glutaraldehyde and incubated for 5 min on ice prior to plunge freezing. Quantifoil R2/2 open-hole grids coated with a layer of freshly evaporated carbon (not covering holes) were glow discharged before applying 4-µl sample onto it. After a 30-s incubation, the grid was double-side blotted using a Vitrobot Mark IV (FEI Thermo Fisher), and then operated at 4 °C at 100% humidity, using a blotting time of 2.5 s.

CMG-polymerase epsilon exo[−] was prepared as follows: freshly glow-discharged 400-mesh lacey grids containing an ultrathin layer of carbon (Agar Scientific) were used for vitrification in a Vitrobot Mark IV (Thermo Fisher) operating at 21 °C and 100% humidity. Samples were vitrified in a double application process. Four microliters of the sample was first applied to the carbon side of the grid and incubated for 120 s. The grid was then double-side blotted for 0.5 s before a further 4 µl sample was applied. After another 120 s incubation, the grid was blotted for 3 s and plunge frozen into liquid ethane.

Data collection. Cryo-EM data for all samples were collected on a Titan Krios EM equipped with a Falcon III direct electron detector (FEI Thermo Fisher) or a K2 Summit direct electron detector (Gatan Inc.) at the Francis Crick Institute. See Supplementary Table 2 for image acquisition details.

Image processing. Pre-processing of deltacat and CMG-polymerase epsilon exo[−] were performed as follows: movie stacks were corrected for beam-induced motion and then integrated using MotionCor2⁶⁰. All frames were retained and a patch alignment of 5 × 5 was used. Contrast transfer function (CTF) specifications for each non-dose-weighted micrograph were estimated by CTFFIND4⁶¹ and Gctf⁶². Good quality-integrated movies examined by Relion-2.1⁶³ were selected for further image processing. Particle picking was performed in a semi-automated mode using e2boxer from EMAN2 (version 2.07)⁶⁴. All further image processing was performed in Relion-2.1.

Deltacat particles were further treated as follows: processing of the Falcon III VPP data were performed as follows. Particle extraction was carried out from dose-weighted micrographs by setting the box size at 184 pixels (pixel size 1.09 Å/pixel). An initial model was generated using cryoSPARC⁶⁵ and was used in processing with Relion-2.1⁶⁶. An initial 816,814 particle dataset was cleaned by 2D classification followed by two subsequent rounds of 3D classification (performing alignment). 3D refinement yielded a 4.45 Å structure, which was filtered to the local resolution using LocRes in Relion-2.1 (Supplementary Table 2 and Supplementary Fig. 1 and 2).

CMG-Pol epsilon exo[−] particles were further processed as follows: a first dataset with a total of 252,705 binned-by-2 particles were extracted from 8,782 dose-weighted micrographs by setting the box size at 256 pixels (pixel size 1.38 Å/pixel) and scaling down to 128 pixels (2.76 Å/pixel) from a first dataset. A second dataset with the same imaging parameters was collected, where a total of 151,971 binned-by-2 particles were extracted from 5,687 dose-weighted micrographs. The particles from the first dataset were subjected to 3D classification with alignment using the negative-stain CMG-polymerase epsilon structure (EMD-6465)²¹ as an initial model (filtered to 60 Å) for five classes. The “ignore CTFs until the first peak” option was selected at this stage and the mask size was set at 350 Å. The best two classes contained a total of 115,068 particles, which were re-extracted back to the unbinned parameters (256 pixels) and subjected to a cascade of 3D refinement

and 3D classification without alignment (see Supplementary Fig. 6). The second dataset was subjected to rounds of 2D classification and the best particles (5671) were re-extracted to unbinned parameters (256 pixel box size) and combined with the 89,809 particles from the first dataset. The merged 95,480 particles were subjected to 3D classification with alignment (three classes) and the best two classes from that step were selected (78,556 particles) and subjected to homogeneous 3D refinement in cryoSPARC⁶⁵. For post-processing, the LocRes function in Relion-2.1 was used by inputting the two unfiltered half maps from the cryoSPARC reconstruction and setting the B-factor to −300 Å.

Molecular modeling. Homology models for yeast C-Pol2 and Dpb2 were generated using HHpred⁴⁰, based on the atomic structure of yeast Pol1 (PDB entry 4FYD)⁴¹ and on the co-crystal structure of human Pole2/ZnF Pole1 (PDB entry 5VBN)³⁴. Rigid-body docking was performed in UCSF Chimera⁶⁷ and manually adjusted in Coot⁴⁸ and subjected to real-space refinement in Phenix⁴⁹. All figures were made using the UCSF chimera⁶⁷.

DNA replication reconstituted in vitro. CMG assembly assays were performed as in ref.². Briefly, MCM was loaded onto 60 ng end-biotinylated DNA fragment containing ARS1 that was immobilized on M-280 streptavidin resin (Sigma) in a 10 µl reaction containing 37.5 nM ORC, 50 nM Cdc6, and 100 nM Mcm2–7-Cdt1. After 10 min at 30 °C, DDK was added to a final concentration 50 nM and the reaction incubated for a further 5 min. Buffer was added to a final concentration of 250 mM K-glutamate, 25 mM HEPES, 10 mM Mg-acetate, 0.02% NP-40-S, 8% glycerol, 400 µg/ml BSA, 5 mM ATP, and 1 mM DTT. A mix of firing factors was assembled immediately before use and added at time 0, to a final concentration of 50 nM Dpb11, 50 nM GINS complex, 50 nM Cdc45, 30 nM Pol epsilon, 20 nM Clb5–Cdc28 (CDK), 2.5 nM Mcm10, 30 nM Sld3–Sld7, and 55 nM Sld2 (firing factor mix). After 10 min at 30 °C, beads were washed twice with a buffer containing 25 mM HEPES 7.6, 5 mM Mg-acetate, 0.02% NP-40-S, 10% glycerol, and 250 mM K-glutamate, resuspended in sodium dodecyl sulfate (SDS)-loading buffer, separated by SDS-PAGE and analyzed by Western blotting with the antibodies indicated.

Replication assays were performed as in ref.⁵², using an 8.2 kb origin-containing DNA template. After 40 min at 30 °C, replication reactions were quenched with EDTA and products separated on a 0.6% denaturing alkaline agarose gel.

Negative-stain EM of the translocating replicative helicase. MCM trains were assembled by activating loaded MCMs on a capped linear DNA segment². Negative-stain sample preparation was performed using carbon coated-300-mesh copper grids (EM resolutions). Grids were glow discharged for 30 s at 45 mA (Electron Microscopy Sciences). Three-microliter drops of nucleoprotein assemblies were applied to the grids and incubated for 1 min. Excess sample solution was blotted away and staining was performed on four separate 70-µl 2% uranyl acetate drops by stirring for 5, 10, 15, or 20 s. Excess stain was blotted away and grids were stored before imaging. Negative-stain micrographs were acquired on a Tecnai LaB6 G² Spirit transmission electron microscope (FEI) operating at 120 keV. Micrographs were collected using a GATAN Ultrascan 100 camera at a nominal magnification of 21,000 (resulting in a pixel size of 4.92 Å), using a defocus range of −0.5 to 2.5 µm. Negative-stain particles were picked using EMAN2⁶⁴, version 2.07, and further image processing was performed in Relion-2.1⁶⁶. Particles were extracted with a box size of 128 × 128 pixels and subjected to reference-free 2D classification with the `–only_flip_phases` additional argument. Size of datasets was as follows: 405 micrographs (75,527 particles) were collected for the MCM train experiment; 228 micrographs (9302 particles) for the multi-site cut/minus methyltransferase control; 112 micrographs (7977 particles) for the single-site cut/minus methyltransferase control; 92 micrographs (4614 particles) for the single-site cut/minus methyltransferase/minus Mcm10 control; 82 micrographs (8013 particles) for the single-site cut/plus methyltransferase/minus Mcm10 control.

Cryo-electron tomography. Twenty tilt series were collected in Tomography 4.0 on a Titan Krios (Thermo Fisher Scientific, Waltham, MA, USA) equipped with a GIF quantum energy filter with a slit width of 20 eV and K2 summit detector (Gatan, Pleasanton, CA, USA). Images were collected from ± 54° with a 3° increment at a pixel size of 2.71 Å. Each exposure received a dose of 3 e/Å² that was fractionated across four movie frames for a total dose of 111 e/Å². The defocus ranged from −5 to −7 µm. Movie frames were aligned with the alignframes function in IMOD and the tilt series was subsequently aligned using fiducial-less patch tracking option in IMOD. 2D CTF correction was performed with ctfphaseself. Tomograms were reconstructed by weighted back-projection and subjected to a SIRT-like filter equivalent to 1 iteration.

Template matching of tomograms was performed with the MOLMATCH software⁵⁵. Individual MCM and CMG maps filtered to 20 Å resolution were used as templates that were systematically rotated and translated before cross-correlation with a region of the tomogram. Euler angle range used for scanning was 0–360 for phi, 0–360 for psi, and 0–180 for theta, with a 10° increment. Missing wedge compensation was applied to the template, therefore constraining the cross-correlation to the experimentally sampled fraction of Fourier space. For each

template, 3D coordinates and orientations that corresponded to the maximum correlation coefficients were extracted using the AV3 toolbox in Matlab (av3_createmotl)⁶⁸. The top MCM and CMG matches were displayed against the tomogram with the EM Package for Amira 5.3⁶⁹ (Thermo Fisher Scientific, Waltham, MA, USA), using the positions and orientations determined by MOLMATCH⁵⁵.

Data availability

Pol epsilon variant deltatcat has been deposited with the EMBD with accession code EMD-0287 and the atomic model with the Protein Data Bank under accession code PDB 6HV8. CMG-Pol epsilon is deposited under EMD entry EMD-0288 and the corresponding atomic model under accession code PDB 6HV9. A reporting summary for this Article is available as a Supplementary Information file. All experimental data are available upon reasonable request.

Received: 6 June 2018 Accepted: 28 October 2018

Published online: 29 November 2018

References

- Pellegrini, L. & Costa, A. New insights into the mechanism of DNA duplication by the eukaryotic replisome. *Trends Biochem. Sci.* **41**, 859–871 (2016).
- Douglas, M. E., Ali, F. A., Costa, A. & Diffley, J. F. X. The mechanism of eukaryotic CMG helicase activation. *Nature* **555**, 265–268 (2018).
- Remus, D. & Diffley, J. F. Eukaryotic DNA replication control: lock and load, then fire. *Curr. Opin. Cell Biol.* **21**, 771–777 (2009).
- Bell, S. P. & Labib, K. Chromosome duplication in *Saccharomyces cerevisiae*. *Genetics* **203**, 1027–1067 (2016).
- Deegan, T. D. & Diffley, J. F. MCM: one ring to rule them all. *Curr. Opin. Struct. Biol.* **37**, 145–151 (2016).
- Remus, D. et al. Concerted loading of Mcm2-7 double hexamers around DNA during DNA replication origin licensing. *Cell* **139**, 719–730 (2009).
- Evrin, C. et al. A double-hexameric MCM2-7 complex is loaded onto origin DNA during licensing of eukaryotic DNA replication. *Proc. Natl. Acad. Sci. USA* **106**, 20240–20245 (2009).
- Abid Ali, F. et al. Cryo-EM structure of a licensed DNA replication origin. *Nat. Commun.* **8**, 2241 (2017).
- Noguchi, Y. et al. Cryo-EM structure of Mcm2-7 double hexamer on DNA suggests a lagging-strand DNA extrusion model. *Proc. Natl. Acad. Sci. USA* **114**, E9529–E9538 (2017).
- Coster, G., Frigola, J., Beuron, F., Morris, E. P. & Diffley, J. F. Origin licensing requires ATP binding and hydrolysis by the MCM replicative helicase. *Mol. Cell* **55**, 666–677 (2014).
- Kang, S., Warner, M. D. & Bell, S. P. Multiple functions for Mcm2-7 ATPase motifs during replication initiation. *Mol. Cell* **55**, 655–665 (2014).
- Bleichert, F., Botchan, M. R. & Berger, J. M. Mechanisms for initiating cellular DNA replication. *Science* **355**, 6327 (2017).
- Yeeles, J. T., Deegan, T. D., Janska, A., Early, A. & Diffley, J. F. Regulated eukaryotic DNA replication origin firing with purified proteins. *Nature* **519**, 431–435 (2015).
- Zegerman, P. & Diffley, J. F. Phosphorylation of Sld2 and Sld3 by cyclin-dependent kinases promotes DNA replication in budding yeast. *Nature* **445**, 281–285 (2007).
- Labib, K. How do Cdc7 and cyclin-dependent kinases trigger the initiation of chromosome replication in eukaryotic cells? *Genes Dev.* **24**, 1208–1219 (2010).
- Deegan, T. D., Yeeles, J. T. & Diffley, J. F. Phosphopeptide binding by Sld3 links Dbf4-dependent kinase to MCM replicative helicase activation. *EMBO J.* **35**, 961–973 (2016).
- Tanaka, S. et al. CDK-dependent phosphorylation of Sld2 and Sld3 initiates DNA replication in budding yeast. *Nature* **445**, 328–332 (2007).
- Itou, H., Shirakihara, Y. & Araki, H. The quaternary structure of the eukaryotic DNA replication proteins Sld7 and Sld3. *Acta Crystallogr. D* **71**, 1649–1656 (2015).
- Muramatsu, S., Hirai, K., Tak, Y. S., Kamimura, Y. & Araki, H. CDK-dependent complex formation between replication proteins Dpb11, Sld2, Pol (epsilon), and GINS in budding yeast. *Genes Dev.* **24**, 602–612 (2010).
- Looke, M., Maloney, M. F. & Bell, S. P. Mcm10 regulates DNA replication elongation by stimulating the CMG replicative helicase. *Genes Dev.* **31**, 291–305 (2017).
- Sun, J. et al. The architecture of a eukaryotic replisome. *Nat. Struct. Mol. Biol.* **22**, 976–982 (2015).
- Abid Ali, F. & Costa, A. The MCM helicase motor of the eukaryotic replisome. *J. Mol. Biol.* **428**, 1822–1832 (2016).
- Ilves, I., Petojevic, T., Pesavento, J. J. & Botchan, M. R. Activation of the MCM2-7 helicase by association with Cdc45 and GINS proteins. *Mol. Cell* **37**, 247–258 (2010).
- Costa, A. et al. The structural basis for MCM2-7 helicase activation by GINS and Cdc45. *Nat. Struct. Mol. Biol.* **18**, 471–477 (2011).
- Abid Ali, F. et al. Cryo-EM structures of the eukaryotic replicative helicase bound to a translocation substrate. *Nat. Commun.* **7**, 10708 (2016).
- Yuan, Z. et al. Structure of the eukaryotic replicative CMG helicase suggests a pumpjack motion for translocation. *Nat. Struct. Mol. Biol.* **23**, 217–224 (2016).
- Langston, L. D. et al. CMG helicase and DNA polymerase epsilon form a functional 15-subunit holoenzyme for eukaryotic leading-strand DNA replication. *Proc. Natl. Acad. Sci. USA* **111**, 15390–15395 (2014).
- Zhou, J. C. et al. CMG-Pol epsilon dynamics suggests a mechanism for the establishment of leading-strand synthesis in the eukaryotic replisome. *Proc. Natl. Acad. Sci. USA* **114**, 4141–4146 (2017).
- Hogg, M. & Johansson, E. DNA Polymerase epsilon. *Subcell. Biochem.* **62**, 237–257 (2012).
- Sengupta, S., van Deursen, F., de Piccoli, G. & Labib, K. Dpb2 integrates the leading-strand DNA polymerase into the eukaryotic replisome. *Curr. Biol.* **23**, 543–552 (2013).
- He, H. et al. Coordinated regulation of heterochromatin inheritance by Dpb3-Dpb4 complex. *Proc. Natl. Acad. Sci. USA* **114**, 12524–12529 (2017).
- Hogg, M. et al. Structural basis for processive DNA synthesis by yeast DNA polymerase varepsilon. *Nat. Struct. Mol. Biol.* **21**, 49–55 (2014).
- Tahirov, T. H., Makarova, K. S., Rogozin, I. B., Pavlov, Y. I. & Koonin, E. V. Evolution of DNA polymerases: an inactivated polymerase-exonuclease module in Pol epsilon and a chimeric origin of eukaryotic polymerases from two classes of archaeal ancestors. *Biol. Direct* **4**, 11 (2009).
- Baranovskiy, A. G. et al. Crystal structure of the human Pol B-subunit in complex with the C-terminal domain of the catalytic subunit. *J. Biol. Chem.* **292**, 15717–15730 (2017).
- Dua, R., Levy, D. L. & Campbell, J. L. Analysis of the essential functions of the C-terminal protein/protein interaction domain of *Saccharomyces cerevisiae* pol epsilon and its unexpected ability to support growth in the absence of the DNA polymerase domain. *J. Biol. Chem.* **274**, 22283–22288 (1999).
- Feng, W. & D'Urso, G. *Schizosaccharomyces pombe* cells lacking the amino-terminal catalytic domains of DNA polymerase epsilon are viable but require the DNA damage checkpoint control. *Mol. Cell. Biol.* **21**, 4495–4504 (2001).
- Nuutinen, T. et al. The solution structure of the amino-terminal domain of human DNA polymerase epsilon subunit B is homologous to C-domains of AAA+ proteins. *Nucleic Acids Res.* **36**, 5102–5110 (2008).
- Handa, T., Kanke, M., Takahashi, T. S., Nakagawa, T. & Masukata, H. DNA polymerization-independent functions of DNA polymerase epsilon in assembly and progression of the replisome in fission yeast. *Mol. Biol. Cell* **23**, 3240–3253 (2012).
- Danev, R., Tegunov, D. & Baumeister, W. Using the Volta phase plate with defocus for cryo-EM single particle analysis. *eLife* **6**, e23006 (2017).
- Soding, J., Biegert, A. & Lupas, A. N. The HHpred interactive server for protein homology detection and structure prediction. *Nucleic Acids Res.* **33**, W244–W248 (2005).
- Perera, R. L. et al. Mechanism for priming DNA synthesis by yeast DNA polymerase alpha. *eLife* **2**, e00482 (2013).
- Isoz, I., Persson, U., Volkov, K. & Johansson, E. The C-terminus of Dpb2 is required for interaction with Pol2 and for cell viability. *Nucleic Acids Res.* **40**, 11545–11553 (2012).
- Johansson, E. & Macneill, S. A. The eukaryotic replicative DNA polymerases take shape. *Trends Biochem. Sci.* **35**, 339–347 (2010).
- Georgescu, R. et al. Structure of eukaryotic CMG helicase at a replication fork and implications to replisome architecture and origin initiation. *Proc. Natl. Acad. Sci. USA* **114**, E697–E706 (2017).
- McGeoch, A. T., Trakselis, M. A., Laskey, R. A. & Bell, S. D. Organization of the archaeal MCM complex on DNA and implications for the helicase mechanism. *Nat. Struct. Mol. Biol.* **12**, 756–762 (2005).
- Lyubimov, A. Y., Strycharska, M. & Berger, J. M. The nuts and bolts of ring-translocase structure and mechanism. *Curr. Opin. Struct. Biol.* **21**, 240–248 (2011).
- Enemark, E. J. & Joshua-Tor, L. Mechanism of DNA translocation in a replicative hexameric helicase. *Nature* **442**, 270–275 (2006).
- Emsley, P., Lohkamp, B., Scott, W. G. & Cowtan, K. Features and development of Coot. *Acta Crystallogr. D* **66**, 486–501 (2010).
- Adams, P. D. et al. PHENIX: a comprehensive Python-based system for macromolecular structure solution. *Acta Crystallogr. D* **66**, 213–221 (2010).
- Frigola, J. et al. Cdt1 stabilizes an open MCM ring for helicase loading. *Nat. Commun.* **8**, 15720 (2017).
- Zhai, Y. et al. Open-ringed structure of the Cdt1-Mcm2-7 complex as a precursor of the MCM double hexamer. *Nat. Struct. Mol. Biol.* **24**, 300–308 (2017).

52. Yeeles, J. T., Janska, A., Early, A. & Diffley, J. F. How the eukaryotic replisome achieves rapid and efficient DNA replication. *Mol. Cell* **65**, 105–116 (2017).
53. Yu, C. et al. A mechanism for preventing asymmetric histone segregation onto replicating DNA strands. *Science* **361**, 1386–1389 (2018).
54. Bellelli, R. et al. POLE3-POLE4 is a histone H3-H4 chaperone that maintains chromatin integrity during DNA replication. *Mol. Cell* **72**, 112–126 e5 (2018).
55. Forster, F., Han, B. G. & Beck, M. Visual proteomics. *Methods Enzymol.* **483**, 215–243 (2010).
56. Sanchez-Pulido, L. & Ponting, C. P. Cdc45: the missing RecJ ortholog in eukaryotes? *Bioinformatics* **27**, 1885–1888 (2011).
57. Lyubimov, A. Y., Costa, A., Bleichert, F., Botchan, M. R. & Berger, J. M. ATP-dependent conformational dynamics underlie the functional asymmetry of the replicative helicase from a minimalist eukaryote. *Proc. Natl. Acad. Sci. USA* **109**, 11999–12004 (2012).
58. Bochman, M. L., Bell, S. P. & Schwacha, A. Subunit organization of Mcm2-7 and the unequal role of active sites in ATP hydrolysis and viability. *Mol. Cell. Biol.* **28**, 5865–5873 (2008).
59. Petojevic, T. et al. Cdc45 (cell division cycle protein 45) guards the gate of the ukaryote replisome helicase stabilizing leading strand engagement. *Proc. Natl. Acad. Sci. USA* **112**, E249–E258 (2015).
60. Zheng, S. Q. et al. MotionCor2: anisotropic correction of beam-induced motion for improved cryo-electron microscopy. *Nat. Methods* **14**, 331–332 (2017).
61. Rohou, A. & Grigorieff, N. CTFIND4: Fast and accurate defocus estimation from electron micrographs. *J. Struct. Biol.* **192**, 216–221 (2015).
62. Zhang, K. Gctf: Real-time CTF determination and correction. *J. Struct. Biol.* **193**, 1–12 (2016).
63. Fernandez-Leiro, R. & Scheres, S. H. W. A pipeline approach to single-particle processing in RELION. *Acta Crystallogr. D* **73**, 496–502 (2017).
64. Tang, G. et al. EMAN2: an extensible image processing suite for electron microscopy. *J. Struct. Biol.* **157**, 38–46 (2007).
65. Punjani, A., Rubinstein, J. L., Fleet, D. J. & Brubaker, M. A. cryoSPARC: algorithms for rapid unsupervised cryo-EM structure determination. *Nat. Methods* **14**, 290–296 (2017).
66. Fernandez-Leiro, R. & Scheres, S. H. Unravelling biological macromolecules with cryo-electron microscopy. *Nature* **537**, 339–346 (2016).
67. Pettersen, E. F. et al. UCSF chimera—a visualization system for exploratory research and analysis. *J. Comput. Chem.* **25**, 1605–1612 (2004).
68. Forster, F. & Hegerl, R. Structure determination in situ by averaging of tomograms. *Methods Cell Biol.* **79**, 741–767 (2007).
69. Pruggnaller, S., Mayr, M. & Frangakis, A. S. A visualization and segmentation toolbox for electron microscopy. *J. Struct. Biol.* **164**, 161–165 (2008).

Acknowledgements

Thanks to Jin Chuan Zhou for help with image processing, to Tom Miller for designing the DNA fork used in fork-affinity purification, Marcus Wilson for help with the DNA-binding experiments, and Peter Cherepanov for help with atomic model building in the early stages of the project. Thanks also to Raffaella Carzaniga and Lucy Collinson (EM STP) for logistic support with the screening microscopes. Phil Walker (Structural Biology STP) for technical support with computing, and access to Krios microscope. Peter Rosenthal for useful discussion on the Volta phase plate. This work was supported by the Francis Crick Institute, which receives its core funding from Cancer Research UK

(FC001065, FC001066), the UK Medical Research Council (FC001065, FC001066), and the Wellcome Trust (FC001065, FC001066). This work was also funded by a Wellcome Trust Senior Investigator Award (106252/Z/14/Z) and a European Research Council Advanced Grant (669424-CHROMOREP) to J.F.X.D. A.C.M.C. is funded by a Wellcome Trust and Royal Society Sir Henry Dale Fellowship (102535/Z/13/Z). F.A.A. and A.J. were supported by a PhD fellowship from the Boehringer Ingelheim Fonds.

Author contributions

P.G., F.A.A., and A.C. designed the study. P.G. and F.A.A. performed all protein–nucleic acid preparations for cryo-EM imaging. A.J. and A.E. generated the yeast strains. P.E. developed the fork-affinity purification protocol and F.A.A. prepared the DNA-CMG-Pol epsilon complex. P.G., F.A.A., J.L., and A.C. prepared and screened cryo grids. A.N., P.G., and F.A.A. collected single-particle data. P.G., F.A.A., and A.C. performed single-particle image processing. A.P., A.C.M.C., F.A.A., and A.C. built atomic models. M.E.D., P.G., F.A.A. J.F.X.D., and A.C. designed in vitro replication biochemical and EM experiments. P. G. purified Pol epsilon variants for in vitro studies and M.E.D. performed in vitro reconstituted replication. F.A.A. performed negative-stain EM experiments on in vitro replication. A.N. collected, reconstructed, and analyzed cryo-electron tomograms. A.C., P.G., and F.A.A. wrote the paper with input from A.N., M.E.D., J.F.X.D., and all other authors.

Additional information

Supplementary Information accompanies this paper at <https://doi.org/10.1038/s41467-018-07417-1>.

Competing interests: The authors declare no competing interests.

Reprints and permission information is available online at <http://npg.nature.com/reprintsandpermissions/>

Publisher's note: Springer Nature remains neutral with regard to jurisdictional claims in published maps and institutional affiliations.



Open Access This article is licensed under a Creative Commons Attribution 4.0 International License, which permits use, sharing, adaptation, distribution and reproduction in any medium or format, as long as you give appropriate credit to the original author(s) and the source, provide a link to the Creative Commons license, and indicate if changes were made. The images or other third party material in this article are included in the article's Creative Commons license, unless indicated otherwise in a credit line to the material. If material is not included in the article's Creative Commons license and your intended use is not permitted by statutory regulation or exceeds the permitted use, you will need to obtain permission directly from the copyright holder. To view a copy of this license, visit <http://creativecommons.org/licenses/by/4.0/>.

© The Author(s) 2018